Journal of Applied Fluid Mechanics, Vol. 18, No. 1, pp. 290-303, 2025.
Available online at www.jafmonline.net, ISSN 1735-3572, EISSN 1735-3645.
https://doi.org/10.47176/jafm.18.1.2651

Effects of Different Attack Angles and Guide Vane Numbers on the Vortex-solid Interaction Noise of Axial Flow Fan

Z. Tu[1], Y. Li[1], J. Zhou[1†] and Z. Chen[2]

[1] *College of Mechanical and Electrical Engineering, Wenzhou University, Wenzhou 325035, Zhejiang, China*
[2] *Key Laboratory of Aerodynamic Noise Control, China Aerodynamics Research and Development Center, Mianyang 621000, Sichuan, China*

†Corresponding Author Email: zhoujxi@wzu.edu.cn

ABSTRACT

This paper utilizes experiments and numerical simulations to investigate the effects of different attack angles of the rotor and the number of guide vanes on the vortex-solid interaction and noise generation of an axial flow fan. The noise and the flow field are measured using far-/near-field microphone arrays and the particle imaging velocimetry (PIV) technique, respectively, conducted in a fully anechoic wind tunnel measuring 0.5m × 0.4m. The numerical simulation uses Large Eddy Simulation (LES). The results reveal that the axial flow fan's noise is all influenced by vortex-solid interaction in various degrees. The angle of attack α changes the noise magnitude by affecting the blades' interaction with the surrounding fluid, causing different pressure pulsations. As the angle of attack α of the rotor blade increases, the tonal noise at the harmonics increases significantly. The increase in noise is partly related to the increment of flow separation caused by the attack angle and partly related to the periodic movement of the rotor blade wake vortex from the front of the static blade to the middle and rear of the static blade. The irregularly distributed static blades reduce the appearance of tonal noise while slightly increasing the work capacity.

Article History

Received February 8, 2024
Revised June 13, 2024
Accepted August 5, 2024
Available online November 6, 2024

Keywords:

Angles of attack
Guide vane number
Noise characteristics
Vortex solid interaction
Axial flow fans

1. INTRODUCTION

The aerodynamic noise mechanism generated by the disturbance of axial flow fans is highly complex, mainly caused by unsteady airflow phenomena such as turbulence, separation flow, and boundary layer flow (Liu et al., 2008a, b). The non-rotating noise in aerodynamic noise is the source of broadband noise in axial flow fans, while the rotating noise is the source of tonal noise (Lu, 1991). Compared to broadband noise, tonal noise can be more than 30 dB higher in sound pressure level, making it a key focus in low-noise design (Longhouse, 1976; Han & Patel, 1977). The portion generated by the dynamic/static interaction between the axial fan rotor blades and the downstream stator in the tonal noise is unavoidable. This phenomenon is due to the interaction between vortices and turbulence wakes generated by upstream blades and the surface of downstream stators, categorizing it as " vortex-solid interaction noise" (Wang, 1972; Chapman & Yates, 1991). Extensive research has been conducted to understand the mechanism behind this type of noise generation (Canepa et al., 2018; Benedek & Vad, 2021; Lewis et al., 2021; Niu et al., 2021; Pereira & Jacob, 2022). Lu et al. (2022) studied the aerodynamic noise characteristics of a 1.5-stage axial compressor through simulations and experiments. The Reynolds-average N-S (RANS) method was used to calculate the shedding-interference noise in a three-dimensional unsteady flow field. Carolus et al. (2007) investigated two prediction methods for broadband noise in low-pressure axial flow fans, with a focus on turbulence-induced shedding-interference noise. Large-eddy simulation (LES) was used to analyze the unsteady blade forces caused by turbulence inflow on the mesh. Zanon et al. (2018) evaluated the calculation methods for broadband noise in a low-speed axial flow fan, predicting the unsteady blade forces induced by high-turbulence inflow using LES. Turbulence statistics for various operating conditions were determined through hot-wire velocity measurement and correlation analysis experiments. Čantrak et al. (2015) and others conducted experimental studies on turbulent vortex flow inside the duct of two different models of industrial axial flow

NOMENCLATURE

α	rotor blade attack angle	$y+$	dimensionless wall distance for the first layer of the wall grid
Z	number of static impellers	u	flow velocity
c	airfoil chord length, mm	v	surface velocity
a	streamwise separation distance between rotor and stator	r	radius of impeller
SPL	Sound Pressure Level	ω	angular velocity
PSD	Power Spectra Density, dB	s	noise source surface
f	frequency, Hz	Ω	fan rotation speed
x, y, z	cartesian coordinates (streamwise, vertical, and spanwise directions), mm	n_1	blade number
O	coordinate plane origin	*SPLi*	the sound pressure level at different frequencies

fans, analyzing the velocity field using SPIV. Liu (2018) simplified the axial flow fan as a pair of tandem airfoils and found that the aerodynamic characteristics of the two airfoils were closest to the optimum state when both airfoils had an angle of attack of 10°.

Additionally, the geometry parameters of the rotor impeller and the upstream structure have a significant impact on the flow field and acoustic field of axial flow fans, which has been a focal point of research in the academic community. Park et al. (2022a) studied the effect of upstream structures on the radiated tonal noise of axial flow fans. The results showed that, under all operating conditions except for high resistance conditions where blade stall occurs, the levels of tonal noise associated with the 1st to 4th components of the Blade Passing Frequency (BPF) were increased for shrouded fans with upstream structures. Liu et al. (2014) investigated the influence of adjustable stator tilting angles on the aerodynamic-structural-acoustic interaction noise of axial flow fans and discussed the unsteady flow and noise characteristics. Simonich et al. (1993) studied the interaction between upstream blades and downstream propellers and compared the magnitude of the vortex-solid interaction noise under different parameter configurations. Li et al. (2022) conducted experimental and numerical investigations on the influence of outer edge bending structures on the aerodynamic performance and sound quality of axial flow fans for air conditioning systems. By using orthogonal design methods, they analyzed the effects of three bending parameters, circumferential start angle, radial relative position, and curvature on the performance of axial flow fan blades, aiming to improve efficiency and reduce noise. Park et al. (2022b) reduced the amplitude of tonal noise associated with the blade passing frequencies by employing forward-swept blades under system resistance conditions, resulting in a noise reduction of 2-4 dBA. Ying (2021) studied the influence of periodic 2D cascades on the broadband noise generated by rotor-stator interaction, such as wake and phase shift parameters.

While there have been many studies in recent years focusing on the influence of different system component parameters on noise characteristics and verifying the noise mechanisms and control techniques through research on various simplified models of axial flow fans, most of the research is still based on analytical or numerical simulations for blade design, lacking comparison with experimental results. In addition, most of the research on vortex-solid interaction noise mechanisms and control focuses on the interference noise between isolated airfoils or simple structures, which are relatively simple and easy to analyze in terms of mechanisms but cannot accurately study the specific noise reduction mechanisms when new structures are applied to axial flow fans, nor accurately evaluate the noise reduction effects.

In this paper, a combination of numerical simulation and experimental methods will be used to investigate the vortex-solid interaction problem in axial flow fans. A model of an axial flow fan equipped with the NACA6412 airfoil will be designed to systematically study the noise characteristics at different angles of attack and analyze its noise reduction mechanism. Since the experiment uses a standard airfoil, the experimental results can provide a research basis for noise analysis, prediction, and reduction in axial flow fans. The expected research outcomes will have a positive impact and practical value for the low-noise design of equipment such as axial flow fans.

The organization of the remaining parts of this paper is as follows. Section 2 describes the experimental environment, test setup, and numerical simulation configuration. Section 3 presents the acoustic and flow field results of the axial flow fan obtained through both experiments and numerical simulations and compares and analyzes the effects of fan configurations. Section 4 presents the conclusions.

2. EXPERIMENTAL SETUP AND SIMULATION METHOD

2.1 Anechoic Wind Tunnel and Models

The experiments were conducted in the laboratory of a fully anechoic wind tunnel at Wenzhou University, which is an open-circuit jet inlet wind tunnel with low background noise and low turbulence levels. The nozzle size is 0.5m (width) x 0.4m (height) and the anechoic chamber size is 4.0m (length) x 3.3m (width) x 3.1m (height). The six walls of the chamber are covered by 0.6 m long fiberglass wedges, which produce 99% sound absorption above 140 Hz (cut-off frequency). The central axis of the tunnel is aligned with the longitudinal direction of the chamber but is off-center in the width direction to allow more space for far-field noise measurements. The

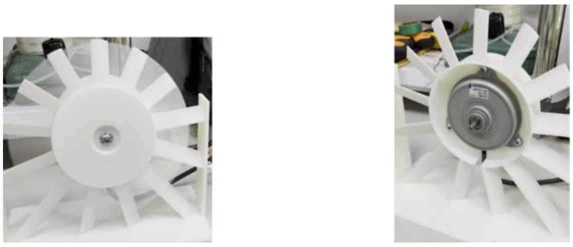

(a) Overall model (rotor rotation)

(b) Motor position

Fig. 1 Experimental model

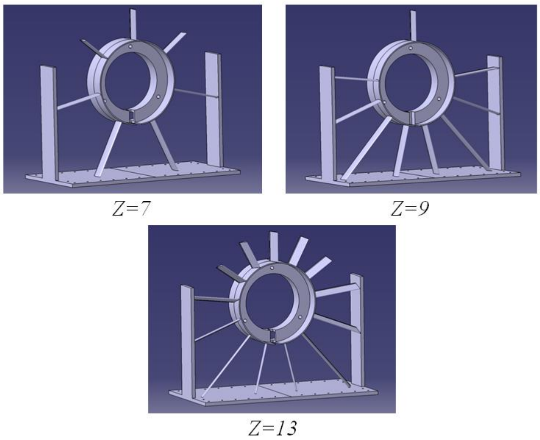

Fig. 2 3D model of stator

wind tunnel setup allowed the distance between the central axis and the wedge to be 1.9 m on one side and 1.4 m on the other.

Figure 1 shows the 3D-printed physical diagram of the axial fan model studied in this paper. The PIV experiment was treated with black matte paint on the surface of the model to avoid reflecting the axial fan model and affecting the experimental results. The model consists of a dynamic impeller with a diameter of 200mm and a hub diameter of 100mm (rotor), a DC motor with a maximum voltage of 12V and a maximum power of 60w, a back-guided impeller (stator) and a bracket with 260mm long, 138mm wide and 170mm high. There are two reasons for choosing the NACA6412 airfoil in this paper, on the one hand, this airfoil has an excellent lift coefficient, on the other hand, applying the airfoil to the design of wind turbine blades is one of the hot research directions at present. On the rotor impeller, the airfoil length is set to 12 mm. Figure 2 shows the 3D model of the three groups of experimental stators. As in Fig. 3, according to the existing literature, the angle of attack of the flow fan rotor impeller is mostly set at about 20° (Liu et al., 2014). In this paper, we define the angle of attack of the rotor impeller blade as α, taking the values 10°, 15°, 20°, 25°, and 30°, and adjust the angle of attack by rotating the airfoil, and then test the noise level. In this paper, in addition to the angle of attack α of the rotor impeller, we also choose the number of stator blade numbers Z as a variable to study the axial fan dynamic and static interaction caused by the vortex solid interaction noise. To intermix with the rotor impeller blade number 11. The number of stator 13 is calculated based on the selection of the ventilator, and the other two experimental groups are calculated within the range of the available stators. The specific model configuration is shown in Table 1.

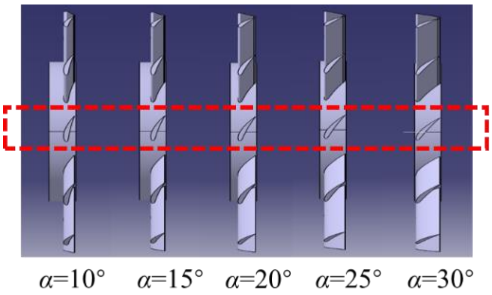

Fig. 3 Setting of the angle of attack

Table 1 Experimental configuration

Static impeller parameters	Rotor parameters
Z=7	α=10°/15°/20°/25°/30°
Z=9	α=10°/15°/20°/25°/30°
Z=13	α=10°/15°/20°/25°/30°

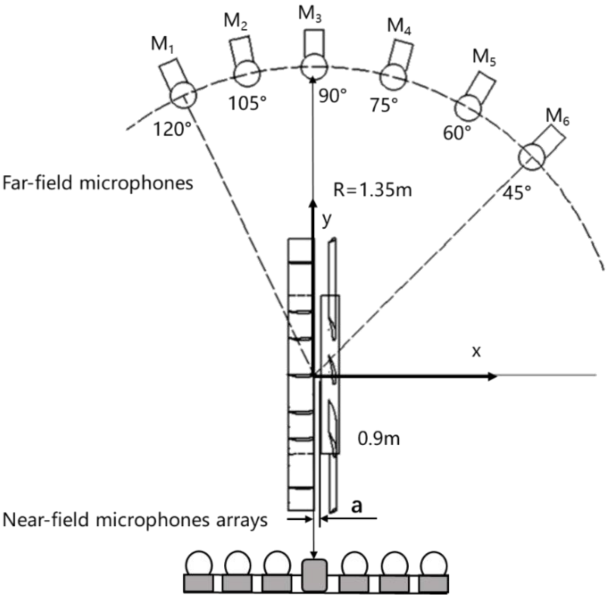

Fig. 4 Two-dimensional schematic diagram of the experimental model and measurement equipment placement

2.2 Experimental Layout

The arrangement and test setup of the model and the noise measuring equipment are shown in Fig. 4 and Fig. 5. A near-field microphone array and a far-field microphone array stand on either side of the test model, where the origin (O) of the Cartesian coordinates (x, y, z) is at the center of the axial flow fan. The x-axis is parallel to the opposite direction of the flow, the y-axis is

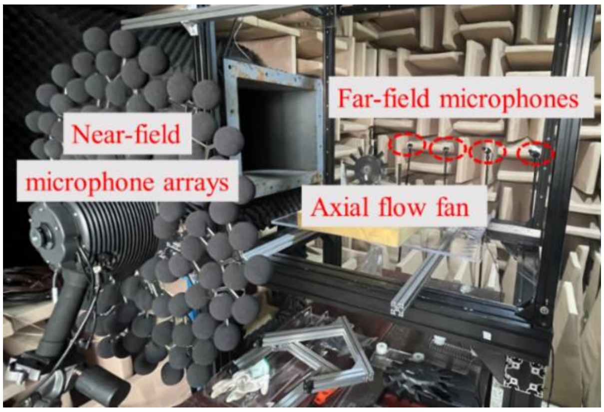

Fig. 5 Placement of equipment for acoustic experiments

perpendicular to the flow, and z is perpendicular to the x-axis and y-axis. The far-field microphone array comprises six microphones (M_1-M_6) that are used to acquire far-field noise signals. The six microphones are arranged at 15° as one position at a distance of 1350mm from the experimental equipment, covering angles from 45° to 120°, numbered M_1-M_6, where M_3 is the main reference object with an angle of 90°, perpendicular to the x-z plane of the experimental object, and M_3 coordinates are (0, 1350, 0). The near-field microphone array is positioned 0.9m from the x-z plane of the tandem airfoils and consists of 112 MEMS microphones, to accurately locate the noise sources. The high-speed camera of the PIV experiment is perpendicular to the z=90 plane, overhead photographing the top of the leaf shunt field.

The far-field microphone, model BSWA MPA201, was connected to a preamplifier providing power, and a data acquisition card, model NI-USB 6529, was used to acquire acoustic data at a sampling frequency of 51,200 Hz and was analyzed in 4096 blocks to obtain a frequency resolution of 12.5 Hz, and the PSD was calculated using Welch’s method with a Hanning window and a block overlap of 50%. A total of 100 blocks were averaged for statistical confidence. For analysis, the time domain signal of the acquired sound pressure was processed in Matlab using the p-welch function. In processing the time domain signal, a Hemming window function was used for each data block to reduce spectral leakage, 100 data blocks were averaged to obtain statistical confidence. The overlap was set to the default value of the function and 51200 data points were selected for a fast Fourier transform with a frequency resolution of 1 Hz. According to the formulae of linear sound pressure level and total sound pressure level, the spectrograms of monitoring points and the total sound pressure levels of different frequency bands are obtained as follows:

$$SPLi = 20lg\frac{P}{P_{ref}} \tag{1}$$

Where $SPLi$ is the sound pressure level at different frequencies, p is the sound pressure value at different frequencies and p_{ref} is the reference sound pressure.

$$SPL = 10\lg\left(\sum_{i=20}^{m} 10^{\frac{SPLi}{10}}\right) \tag{2}$$

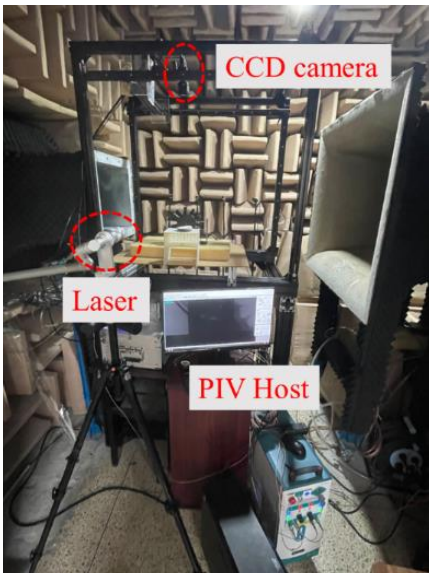

Fig. 6 Placement of equipment for PIV experiments

Where SPL denotes the total sound pressure level and i and m denote the start and cut-off calculation frequencies respectively.

The acoustic signals from the near-field microphone array were recorded with a sampling rate of 48 kHz for 8s and analyzed using a block size of 2048, yielding a frequency resolution of about 24 Hz. The acquired data were post-processed using the eigenvalue-optimized beamforming algorithm to locate the noise sources.

Figure 6 shows the schematic particle image velocimetry (PIV) test setup for flow field measurements. The laser used in this paper is a double-pulse type (New Wave Gemini Neodymium-Doped Yttrium Aluminum Garnet (Nd: YAG)), with a maximum energy of 120 mJ and a laser sheet thickness of about 1 mm in the model area. A Nikon charge-coupled device camera with a resolution of 2456 × 2672 pixels was used to capture the images. The camera was placed directly above the fan, and a laser, which is focused on the top of the fan blades, was placed on the side of the fan. The main purpose of the flow field experiment is to show the flow structure between and around the rotor and the stator. Due to the stator blades blocking the laser light, the camera is unable to capture particles in this region.

2.3 Numerical Simulation Method

In the numerical simulations conducted for this study, the ANSYS Fluent software was utilized. The turbulence model selected for the simulations was the LES model, which is well-suited for capturing turbulent flow phenomena. The core concept of LES involves utilizing direct numerical simulation to compute vortex kinematics influenced by boundary conditions. Additionally, the grid model is employed to simulate small vortices occurring at relatively high frequencies, as well as to calculate relatively small eddy currents at a higher frequency. The LES simulation method is utilized by researchers to simulate and compute complex turbulence present in wind turbines. This approach overcomes the limitations of the RANS method, which cannot effectively simulate blade

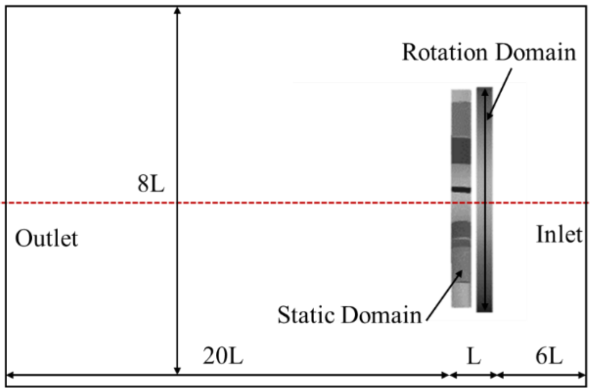

Fig. 7 Two-dimensional schematic of numerical simulation

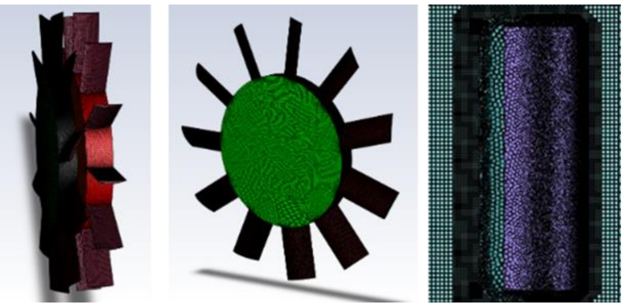

Fig. 8 Axial flow fan model ((a)stator、(b) rotor、(c) airfoil)

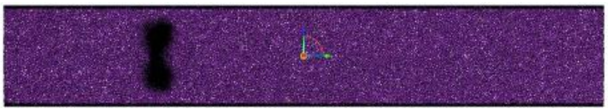

Fig. 9 Computational domain meshing

separation or the interaction between adjacent blades. LES simulation accurately and efficiently addresses the issue of free turbulence on the wind turbine blade surface, providing comprehensive flow field information within the wind turbine. It serves as an important tool for studying wind turbine noise. The SIMPLE algorithm is used to solve the coupled pressure-velocity equations, where the equations are in a second-order center difference format for the convective terms and a second-order windward format for the diffusive terms.

Figure 7-9 shows the two-dimensional schematic diagram of the computational domain for the numerical simulation. The computational domain is divided into the inlet, outlet, rotor rotation domain, static sub-static domain, and surrounding air region, where L is the total axial width of the axial fan rotor and static sub-static, extending 6L forward for the inlet domain and 20L backward for the outlet domain; the overall computational domain is a cylinder with a diameter of 8L. Fluent Meshing software was used to generate near-wall polyhedra and far-field hexahedral meshes. LES model is used for calculation, so the minimum spacing in the direction normal to the surfaces of the rotor and the stator is set to be 0.005 mm respectively to assure that the turbulent unit y+ is less than 1. To reduce the number of meshes, larger mesh sizes are used in areas away from the model, but not exceeding a maximum of 0.5mm. The number of meshes is about 4 million, and its mesh quality is controlled above 0.7. The inlet and outlet boundary conditions are set to pressure inlet and pressure outlet, respectively, with an initial value of pressure equal to 1 atm. The rotor and static boundary conditions are set to wall, where the rotation of the rotor is in the form of grid rotation and a speed of 2510 revolutions per minute is added. The boundaries surrounding the stationary domain are defined as wall.

To solve the coupled pressure-velocity equation, a coupled algorithm was employed. The convective term of the equation was discretized using a second-order central difference format, while the diffusive term was discretized using a second-order windward format. This approach ensures accurate and stable numerical solutions. For the far-field noise calculation, the Ffowcs Williams-Hawkings (FW-H) equation was used. Ffowcs Williams and Hawkins applied the generalized functional method to consider the effect of moving solid boundaries on acoustic waves, i.e., the presence of moving objects in fluids, and derived the FW-H equation, from which it follows that fluids and moving objects can interact with each other.

Two noise sources were considered in the simulations: the rotor impeller and the static blades. The time step used in the simulations was set to 6.64×10-5 seconds (This value is the time per degree of rotation of the rotor), and the sampling frequency for data acquisition was set to 15 kHz. By employing these numerical simulation settings and methodologies, the researchers were able to gain insights into the flow field behavior and noise generation mechanisms associated with the vortex-solid interaction in axial fans equipped with NACA6412 airfoils.

3. RESULTS AND ANALYSIS

3.1 Effects of Attack Angle (α) on Vortex-Solid Interaction Noise

This paper examines the interaction mechanism of noise between axial fan rotors and stators at various angles of attack (α) from both pneumatic acoustics and aerodynamics perspectives. The subsequent sections present the results of the far-field noise experiment, the near-field microphone noise localization, and the flow field information obtained through the PIV experiment. To minimize the experimental error, the noise spectrum and the size of the noise decibel value are averaged after three repetitions of the test.

Figure 10 presents a comparison of the noise Power Spectral Density (PSD) of the axial fan models at different angles of attack when the rotation speed is 2510rpm (the highest fan speed that can be achieved under the rated voltage of the motor in this experiment), measured at the far-field noise measurement point M_3(y=1350mm). Upon examining the data in the figure, it is evident that the experimentally obtained peak noise frequency aligns well with the BPF and its harmonic frequencies, indicating that the noise generated by the blade passage frequency and its

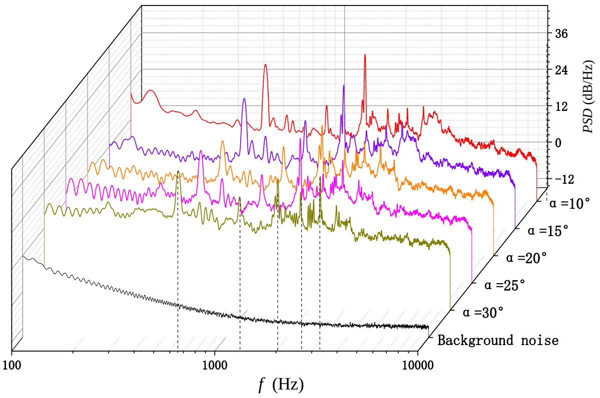

Fig. 10 Baseline model (*Z*=13) axial fan far-field noise spectrum

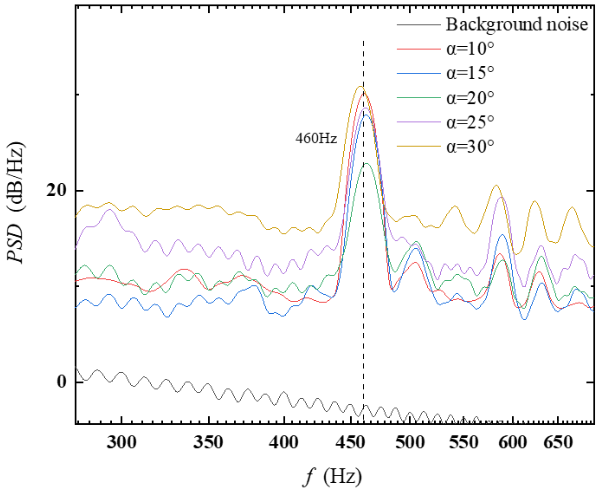

Fig. 11 Baseline model (*Z*=13) axial fan far-field noise spectrum

harmonics. The theoretical value of blade can be calculated using the formula: BPF = $\Omega n_1/60$ = 460 Hz, where Ω represents the fan rotation speed, and n_1 refers to the number of rotor blades. Comparing the experimental results for different attack angles *α*, it is evident that the 30° attack angle group exhibits higher noise amplitude across all frequency bands. As the attack angle *α* decreases, the noise amplitude decreases progressively, with a more significant reduction in broadband noise between harmonics compared to tonal noise. Notably, the noise level in the experimental group with the lowest attack angle (*α* = 10°) surpasses some of the other groups in the middle and low-frequency bands (as shown in Fig. 11). This intriguing observation will be further discussed within the context of the numerical simulation section.

Figure12 and Fig.13 present the 200ms average flow field velocity and vortex obtained from PIV experimental measurements of the axial fan flow at various angles of attack: (a) *α*=10°, (b) *α*=20°, and (c) *α*=30°. The flow field at and above the suction surface of the static blade could not be captured by the high-speed camera due to the laser being obscured by the blade, so the time-averaged results of the flow field in this part could not be compared.

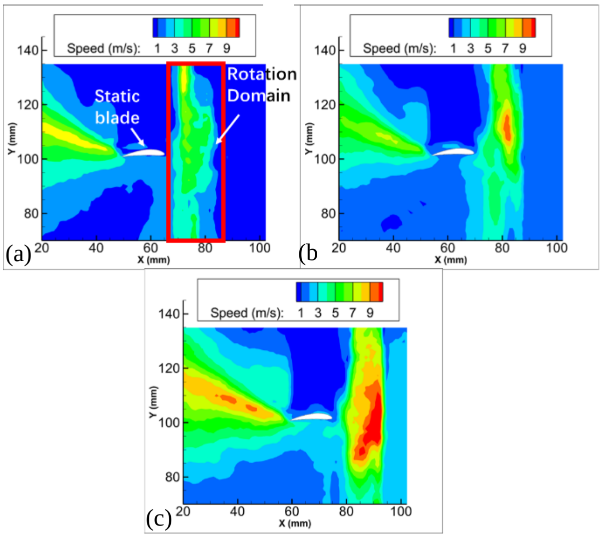

Fig. 12 Experimental speed contour of axial fan 2510rpm PIV with different angle of attack reference models ((a)*α*=10°、(b) *α*=20°、(c) *α*=30°)

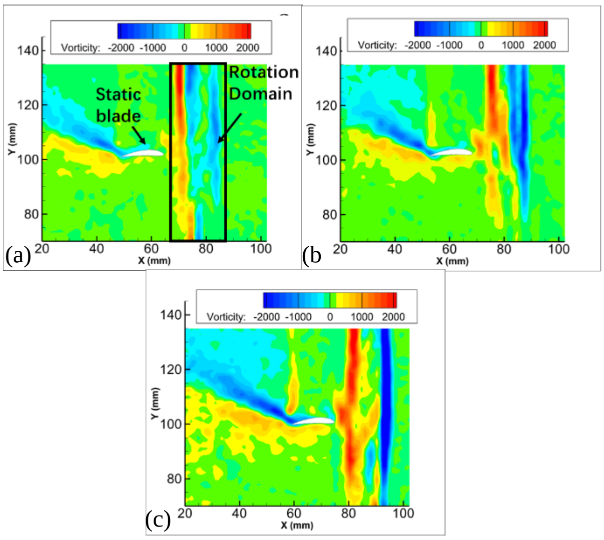

Fig. 13 Vortex contour of axial fan 2510rpm PIV experiment with different angle of attack reference models ((a)*α*=10°、(b) *α*=20°、(c) *α*=30°)

It is evident that at an attack angle of 10°, the rotational speed of the upstream blade region is relatively low, resulting in minimal interaction with the downstream static components. As the attack angle increases, a noticeable mutual interaction is observed within the rotating region. This can be attributed to the increased windward attack angle of the upstream rotor impeller blade, which leads to a larger windward area and the development of a velocity difference between the fluid on the windward side (pressure side) and the leeward side (suction side) of the upstream rotor impeller blade. Consequently, this gives rise to the formation of a larger vortex cloud. Additionally, the shedding vortex from the upstream rotor impeller impacts the downstream airfoil, resulting in increased vorticity on the top surface of the static sub-airfoil as well as on the static pressure surface.

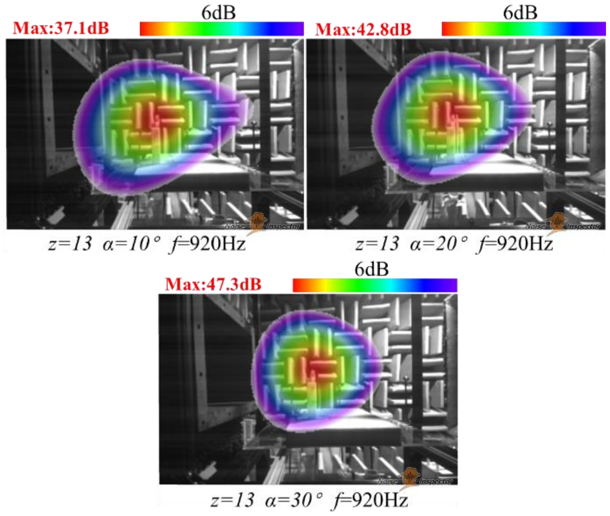

z=13 α=10° f=920Hz z=13 α=20° f=920Hz

z=13 α=30° f=920Hz

Fig. 14 Baseline model (*Z*=13) second-order harmonic source localization map with different attack angles

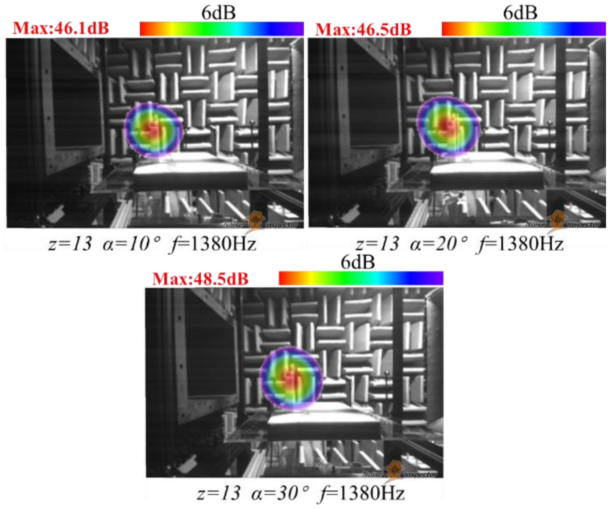

z=13 α=10° f=1380Hz z=13 α=20° f=1380Hz

z=13 α=30° f=1380Hz

Fig. 15 Baseline model (*Z*=13) third-order harmonic source localization map with different attack angles

Figure 14 and Fig. 15 illustrate a comparison of the near-field sound source locations at the second and third-order harmonic positions of the benchmark model under different attack angles. The right side of the diagram represents the rotor, while the left side represents the stator. Therefore, the flow direction in the diagram is from right to left. It is noted that the sound source locations at the BPF are not included in this comparison due to their lower frequency and wider sound source locations. Upon examining the sound source localization diagrams at different attack angles, it becomes apparent that the noise sources at higher angles of attack exhibit a slight upstream shift compared to those at lower angles of attack. This observation, in conjunction with Fig. 11, suggests that this phenomenon could be attributed to the following factors: At low angles of attack, the dominant contributors to noise are the wake noise and impeller rotation noise. These sources primarily occupy the main body region. However, as the angle of attack increases, the vortex-solid interaction between the rotor and stator intensifies. Consequently, there is an increase in the vortex volume on the top surface of the static airfoil as well as on the pressure surface of the stator. This increase in vortex volume reduces the influence of the wake noise from the stator on the sound source localization. As a result, the sound source shifts upstream of the airflow.

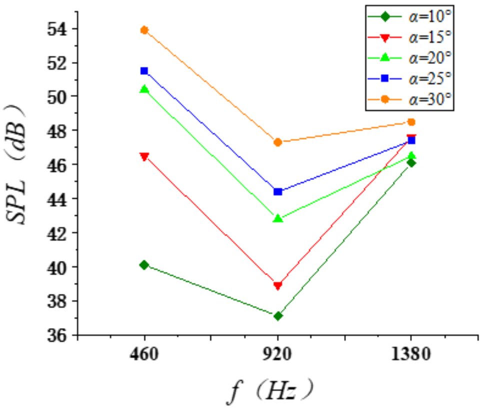

Fig. 16 Comparison of different attack angles through BPF and second/third order harmonic peak noise for baseline models

Figure 16 compares the baseline model pass-by frequency and second/third-order harmonic frequency peak noise at different angles of attack obtained from the near-field microphone array. From the observation, it is evident that at higher angles of attack, there is consistency in the noise changes across different frequencies. However, at lower angles of attack, there is a significant decrease in noise specifically at the BPF, with a shift in dominant noise from BPF to third-order harmonic noise. The sensitivity of the noise change at the BPF is significantly larger than that of the harmonic noise with the increase of the angle of attack, so future noise reduction work can be centered around the reduction of the first-order harmonic noise.

3.2 Effects of Guide Vane Numbers (*Z*) on Vortex-Solid Interaction Noise

To investigate the impact of the static impeller on the vortex-solid interaction noise, a 7-guide blade (*Z*=7) and a 9-guide blade experimental model (*Z*=9) were established in this study. As depicted in Fig. 11, the baseline model (*Z*=13) exhibits noise and has a wide distribution range at the 460Hz BPF. However, the second-order harmonic (920Hz) is predominantly located at the top of the static impeller, while the third-order harmonic (1380Hz) gradually shifts towards the bottom of the static impeller. Comparing the baseline model with the 9-guide vane control model along with the far-field noise spectrum of the axial fan for different models illustrated in Fig. 17, the lack of guide vane in the upper part of the static impeller makes the sound source at the BPF and harmonics have different degrees of downward shift, and the noise decibel value decreases (Fig.18), which indicates that the BPF and the harmonic noise are affected by the interaction of vortex-solid between rotor and stator.

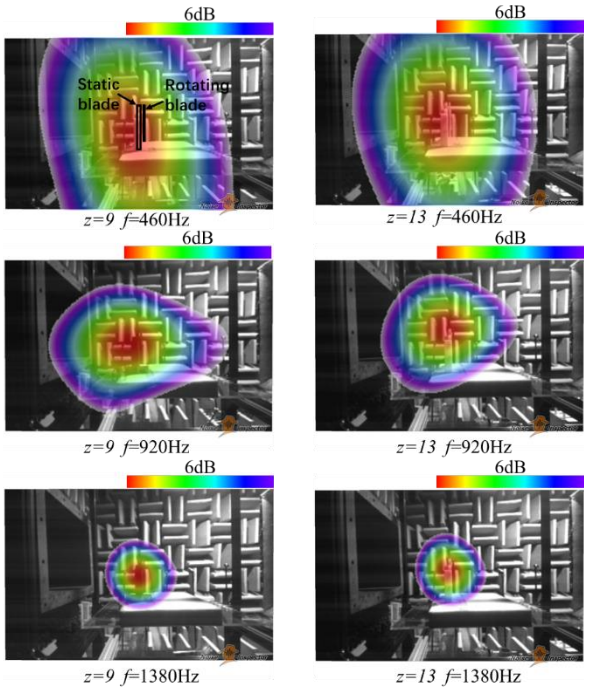

z=9 f=460Hz *z=13 f*=460Hz *z=9 f*=920Hz *z=13 f*=920Hz *z=9 f*=1380Hz *z=13 f*=1380Hz

Fig. 17 Sound source localization diagram at axial fan BPF and harmonic frequency for Asymmetric 9 guide vane model (*Z*=9) and baseline model (*Z*=13)

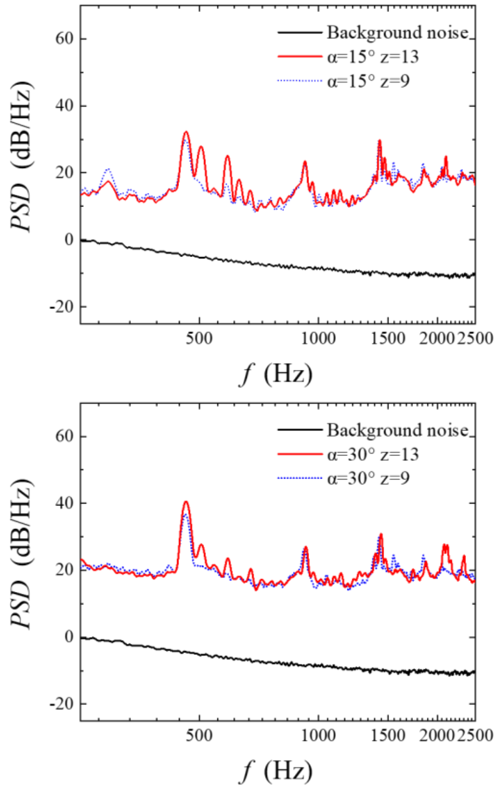

Fig. 18 Axial fan far-field noise spectrum for asymmetric 9 guide vane model (*Z*=9) and baseline model (*Z*=13)

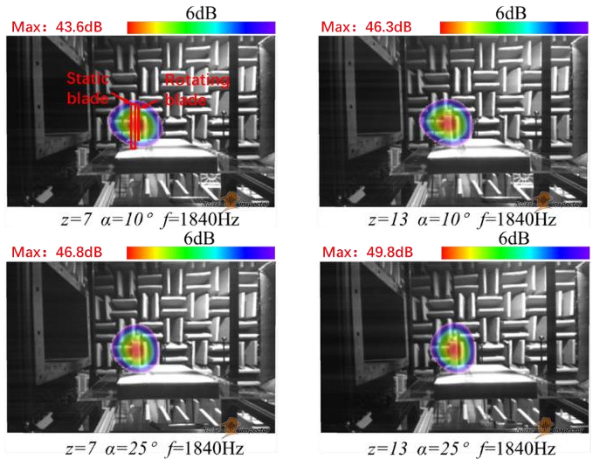

z=7 α=10° f=1840Hz *z=13 α=10° f*=1840Hz *z=7 α=25° f*=1840Hz *z=13 α=25° f*=1840Hz

Fig. 19 Axial fan 7 guide vane and 13 guide vane models with different angles of attack fourth-order harmonic (1840Hz) frequency at the sound source localization map

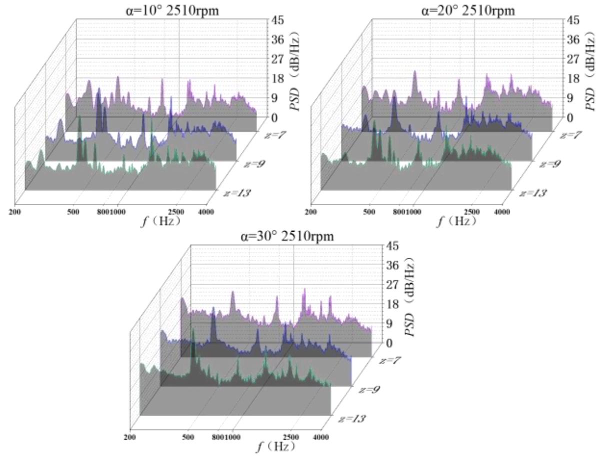

Fig. 20 Far-field noise spectrum of each experimental model with the same angle of attack *α*

In Fig. 19, the sound source location map at the fourth-order harmonic frequency (1840 Hz) is presented for axial fan models with different numbers of guide vanes and angles of attack. Comparing the left and right diagrams, it is evident that evenly increasing the number of guide vanes does not alter the sound source location. However, the noise pressure level increases by approximately 3 dB, indicating that the fourth-order harmonics are still influenced by vortex-solid interaction noise between the rotor and the stator.

Figure 20 presents the far-field noise spectrograms for three different sets of guide vane numbers (*Z*=7, *Z*=9, *Z*=13) of the experimental model, all under the same rotor impeller blade attack angle. The spectrograms reveal distinct monotonous noises occurring at the BPF (460 Hz), second harmonic (920 Hz), and third harmonic (1380 Hz) positions. Notably, the baseline model exhibits significantly higher amplitudes of both the tonal noise and broadband noise compared to the control groups (*Z*=7 and *Z*=9). This is attributed to the denser distribution of guide vanes in the baseline model, leading to more intense interaction between the rotor impeller and the stator. Moreover, it is observed that the *Z*=13 baseline model

Table 2 BPF and second/ third order harmonic frequency peak noise (dB) for models with different guide vane numbers

Guide vane numbers	BPF 460Hz	Second-order harmonic 920Hz	Third-order harmonic 1380Hz
Z=7	52.1	44.9	46.8
Z=9	51.8↓	44.3↓	46.5↓
Z=13	53.9	47.3	48.5

produces more prominent wave clusters in the broadband noise region between the first and second-order harmonics compared to the *Z*=7 and *Z*=9 control groups.

Meanwhile, combining the data in Table 2, comparing the *Z*=9 group with the *Z*=7 and *Z*=13 groups, the irregular distribution of static blades suppresses some noise peaks. However, comparing the *Z*=7 group with the *Z*=9 group, despite the increase in the number of guide vanes, the BPF noise and the harmonic frequency noise of the *Z*=9 group are lower than that of the *Z*=7 group.

3.3 Numerical Simulation

The number of grids plays a very important role in numerical simulation. The larger the number of grids, the more accurate the results of numerical simulation usually are, but the more resources are required for the calculation. In numerical simulation, not only the grid itself takes up a part of the memory, but also the data files generated by the computation will take up a large amount of memory. In addition, the CPU computation time is proportional to the number of grids because each computational cell is solved during the simulation. To obtain a more accurate calculation result and save computational resources, it is especially important to perform the sensitivity verification of the grid.

In this section, the baseline model (α = 30°, Z = 13, Ω = 2510 rpm) is selected for sensitivity validation of the grid. The baseline model is divided by polyhedral grids, and three different grid numbers are considered, namely 2M, 4.2M, and 8.2M.

The comparison of the noise power spectral density and the total sound pressure level of the four noise monitoring points and the trend of the change of the values in different grids is used to validate the sensitivity of the grids. Figure 21 and Fig. 22 give the comparison results of the noise spectrogram at noise monitoring point M3 and the numerical magnitude of the total sound pressure level and the changing trend of the four noise monitoring points for the baseline model at different grid numbers, respectively. For the baseline model, it can be seen that when the number of grids is 2M, although it can simulate the monotone noise at the passing frequency of the wind turbine blades, its noise spectrum at the broadband noise is low compared with the values of the 4.2M and 8.2M groups. Comparing the case when the number of grids is 4.2M and 8.2M respectively, the frequency peaks are almost constant and the noise at the small spikes at the broadband noise frequency band is also better conformed. From the four noise monitoring points of the total sound pressure level numerical size and the trend of change can also be found, the grid number of 2M and the grid number of 4.2M and 8.2M results have obvious deviation, while the latter two of the total sound pressure level size and the trend of change is also basically the same, indicating that the use of the grid number of 4.2M to calculate the sound field of the axial fan model is sufficient to meet the requirements of the accuracy of the calculation. Therefore, to save the calculation cost, the numerical simulation in this chapter selects the grid number of 4.2M to calculate the axial fan model and the noise control strategy model.

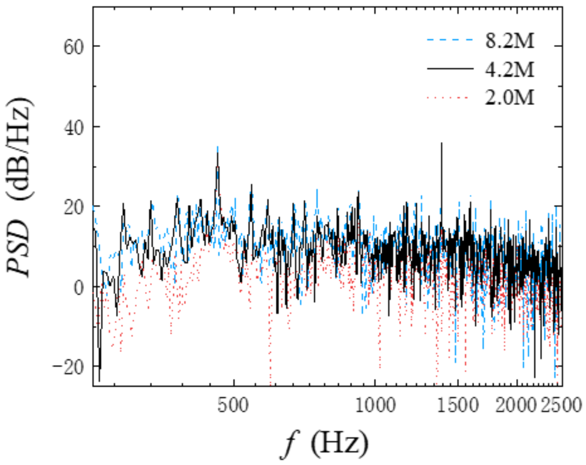

Fig. 21 Comparison of far-field noise spectra of baseline models of axial fan with different number of meshes

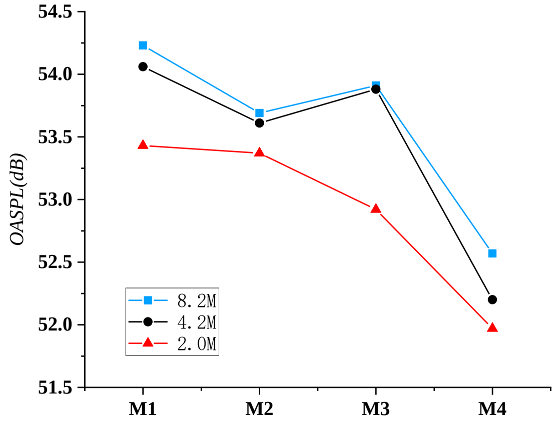

Fig. 22 Comparison of far-field total sound pressure level of axial fan baseline model with different number of grids

The numerical simulation of the constant state was carried out before the simulation of the non-constant flow, which not only helps to speed up the simulation of the non-constant flow state but also checks whether there is any problem with the initial setup. Equation (3) gives the formula for the rotational linear velocity v of the fan, r denotes the radius of the axial fan, and *w* denotes the angular velocity.

$$v = r\omega = \frac{2\pi\Omega}{60} \times 0.1 = 26.3(m/s) \tag{3}$$

Figure 23 illustrates the average velocity cloud for

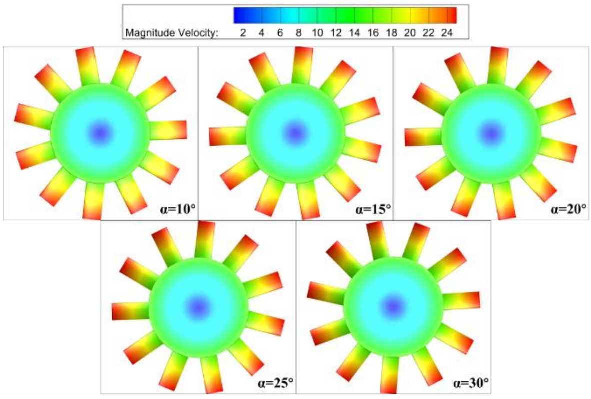

Fig. 23 Numerical simulation velocity contour of axial fan rotor impeller surface ((a)α=10°、(b) α=15°、(c) α=20°、(d) α=25°、(e) α=30°)

different models operating at their design speed Ω = 2510 rpm. It can be seen that the numerically computed linear velocities at the edge of the rotating outer ring of the baseline model and the theoretically computed values match well. To further verify the accuracy of the numerical simulation, the velocity cloud diagrams of the rotor impeller of the axial fan under different angles of attack are provided, and the results are all consistent with the theoretically calculated values. At the same time, it can be found that the high-speed region of the fan blade rotation is mainly concentrated in the top trailing edge region of the fan blade, which will have a strong interaction with the downstream static sub-blade, and this part will be analyzed in the subsequent development. The preliminary analysis of the axial fan rotor impeller velocity cloud diagram, can to a certain extent prove the reliability of the numerical simulation, which later will be compared with the numerical simulation of the sound field results through the noise experiment, to further prove the reliability of the numerical simulation in this paper.

Figure 24 compares the cloud diagram of the vorticity distribution of the mean flow field during the model experiment and numerical simulation. It can be seen that the pressure surface of the static sub-blade and the development trend of the wake vortex clusters in the vorticity cloud map are in better conformity. Among them, the suction surface and the backflow field particles (the black boxed part on the left) cannot be captured by the high-speed camera due to the blocking of the laser by the experimental static impeller blades; meanwhile, the time-averaged results of the flow field in this part cannot be compared because the rotor impeller grid (the red boxed part on the right) cannot be time-averaged balanced in this region due to the rotating motion changing all the time during the numerical simulation.

Figure 25 compares the PSD obtained from the axial fan experiment with the numerical simulation of the far-field noise measurements (baseline model), specifically at the far-field microphone M_3. The PSD curve from the numerical simulation aligns well with the experimental data at the BPF and the second harmonic, indicating a certain level of reliability for the numerical simulation. However, it is important to note that the overall level of broadband noise in the numerical simulation is low. This could be attributed to the exclusion of motor noise and mechanical vibration noise in the numerical model.

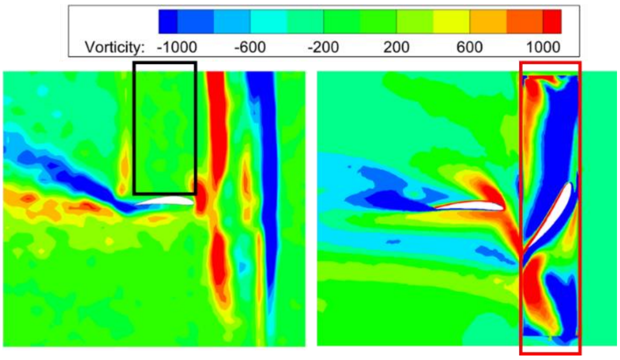

Fig.24 Comparison of eddy time-averaged results between the baseline model experiment (a) and numerical simulation (b)

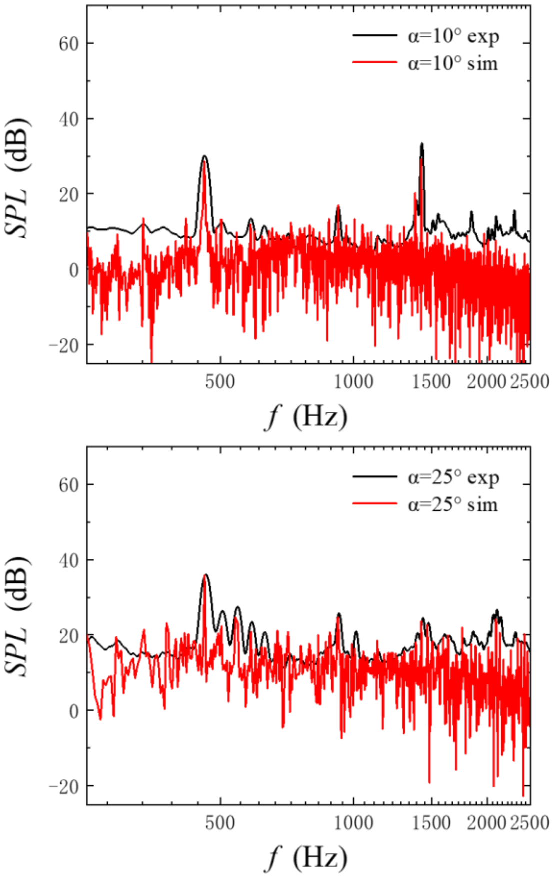

Fig. 25 Experimental and numerical simulations of the SPL spectrum of the sound field for Z=9 ((a)α=10° 、(b) α=25°)

Figure 26 illustrates the pressure and vortex diagrams obtained from the numerical simulation of the baseline model at 90% of the blade height. The diagrams represent different rotor impeller blades with varying angles of attack (α) and their relative positions to the static sub-blades. From left to right in the figure, we can observe the changing relative positions of the rotor blade and the static impeller. At attack angle α of 10°, a more pronounced

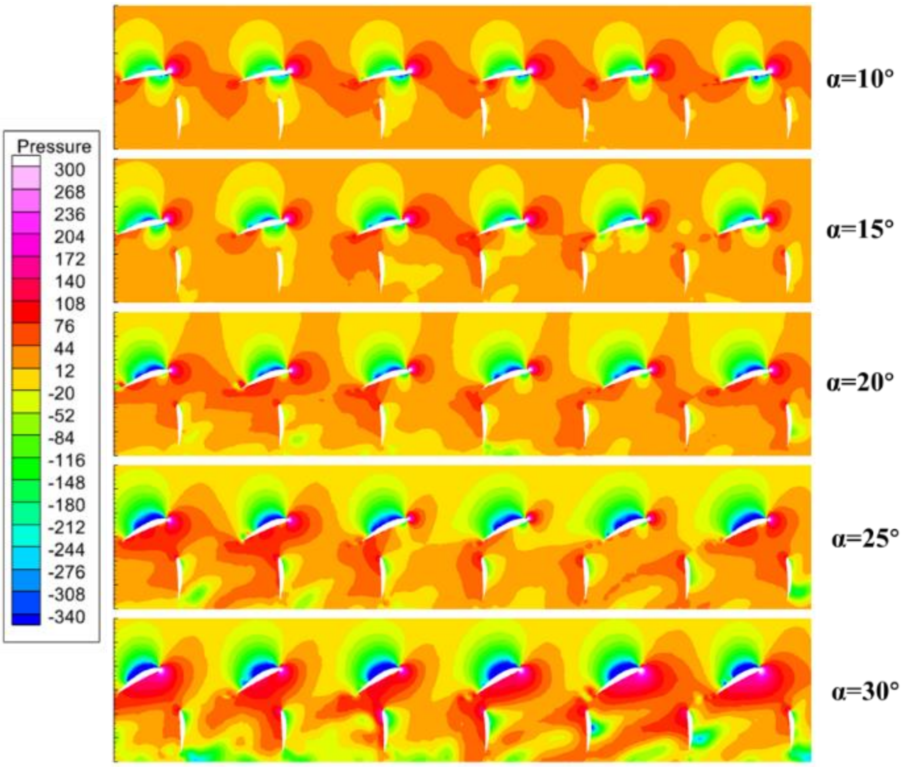

Fig. 26 Contour plot of pressure distribution at 90% of the blade height cross-section for the baseline model rotor impeller at different *α* ((a)*α*=10°、(b) *α*=15°、(c) *α*=20°、(d) *α*=25°、(e) *α*=30°)

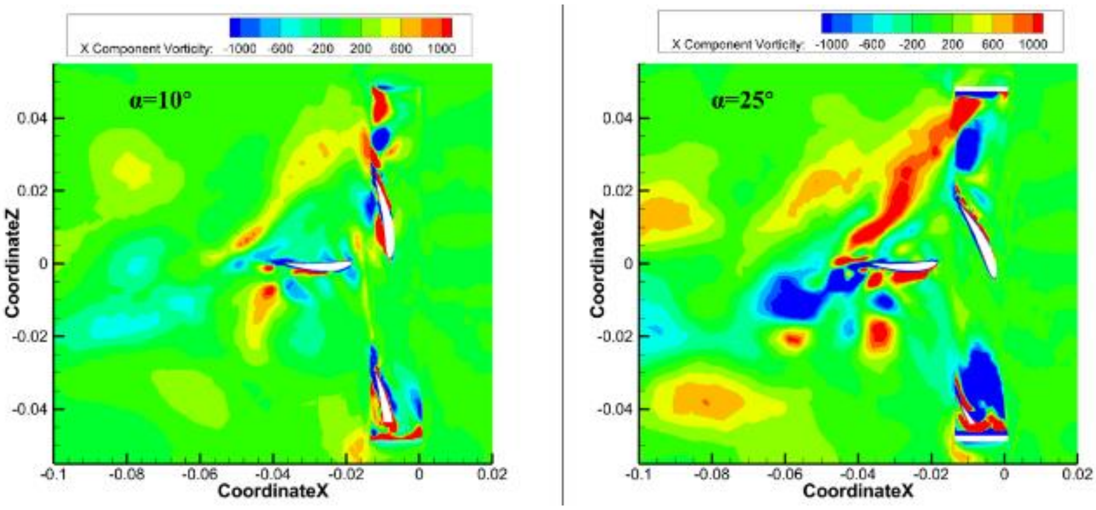

Fig. 27 Contour plot of vortex distribution at 90% leaf height section of rotor impeller with a different attack angle ((a) *α*=10°、(b) *α*=25°)

negative pressure zone is formed ahead of the pressure front of the rotor impeller blade. By referring to Fig. 27, we can infer that this negative pressure area is a result of the low angle of attack, small airflow direction, and airfoil chord angle. These factors contribute to the heightened separation flow at the tip of the axial fan blade, causing the formation of a separation vortex at the leading edge of the blade's pressure front (This may also be the reason why the tonal noise of axial flow fans increases at low attack angles). Consequently, a negative pressure is generated. As the angle of attack increases, the blade tip separation vortex diminishes. This disappearance of the vortex may be attributed to the larger angle of attack, which leads to a reduction in tonal noise produced by the axial flow fan. Additionally, as the rotor blade periodically interacts with the stator in different relative positions, a periodic change in pressure occurs on the suction surface of the static sub-blade. This pressure change region gradually moves backward as the rotor impeller blade moves away from the suction surface. The periodic excitation of the rotor and the airflow between the rotor and the stator as the impeller rotates freely, coupled with interactions with the downstream stator, give rise to periodic interaction. This results in the formation of vortex groups moving

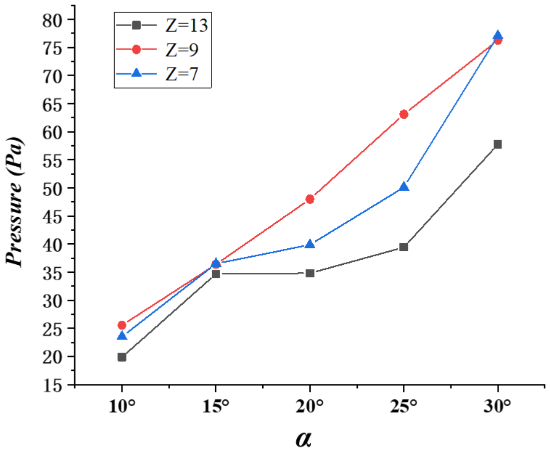

Fig. 28 Comparison of the values of total pressure on the outlet surface for different static impellers at different rotor impeller angles of attack

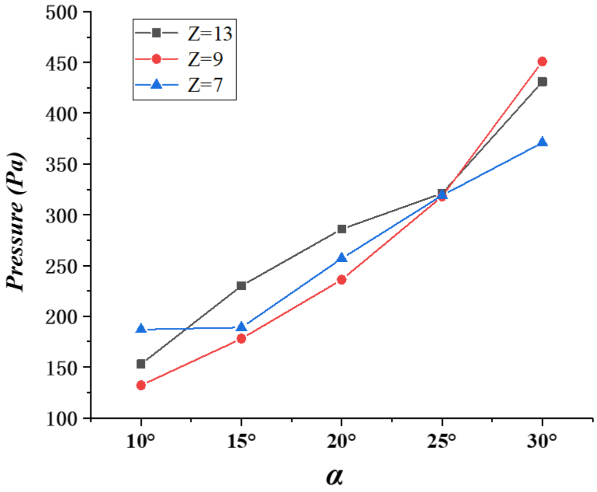

Fig. 29 Surface maximum full pressure of three sets of stators at different angles of attack

periodically along the suction face of the stator, contributing to the periodic pressure changes in the vicinity of the blade near the wall surface. Combined with the comparison of the noise spectra in Fig. 10 and the total sound pressure level of the noise in Fig. 16, the reasons for the increase of noise in the experimental group of the high angle-of-attack are mainly two parts. On the one hand, the high angle of attack leads to the formation of a large number of vortex structures around the rotor blades, and on the other hand, a large number of rotor blade wake vortices impinge on the downstream stator, leading to the emergence of larger-scale vortex structures around the top of the downstream static blade and the pressure surface. In addition, the reason for the abnormally elevated noise in the low-frequency band for the low angle of attack experimental group is believed to be caused by the increase of vortices separating from the leading edge of the blades.

Figure 28 and Fig. 29 demonstrate the comparison of the values of total pressure on the outlet surface and total pressure on the surface of the static impeller for different static impellers at different rotor impeller angles of attack. It can be seen that at lower angles of attack (α = 10°, 15°), the total pressure at the outlet section of the five groups of axial fans is close to each other. With the increase of the angle of attack, the total pressure on the outlet surface of the guide vane group (Z=9) is larger than that of the other two groups, which shows that the guide vane group (Z=9) has more excellent work capacity; Comparing the total pressure on the pressure surface at different angles of attack for the three groups of static impellers in the right figure, the asymmetric guide vane group has a lower total pressure at the three lower angles of attack. At the angle of attack α=25° the total pressure values of the three groups are similar. At the angle of attack α = 30°, the total pressure of the asymmetric guide vane group is higher than that of the other two groups. Combined with the comparison of the total pressure in the outlet section and the full pressure on the static impeller pressure surface, it can be found that below the angle of attack α = 25 °, at the same time, the asymmetric guide vane group (Z = 9) fans in the work capacity is more powerful, the rotor impeller on the static impeller pressure impact is smaller, which can reduce the static impeller strength requirements, so that the static impeller blade material selection can be more extensive and lower cost.

4. CONCLUSION

In this paper, the vortex solid interaction phenomenon of an open-type low-speed axial fan equipped with a NACA6412 airfoil is investigated using a combination of experimental and numerical simulations, taking into account the combined effect of the rotor impeller blade angle of attack and the number of static sub-blades. Near- and far-field noise measurements and PIV measurements were performed in an experimental wind tunnel. The measured results show that the angle of attack and the number of guide vanes can affect the performance of the pressure, velocity, and vortex structure of the flow field of the fan to a certain extent. The main conclusions can be summarized below：

(1) The experimental results with different angles of attack show that the noise amplitude of each group increases as the angle of attack α increases. In addition to the tonal noise at harmonic frequencies, the broadband noise between harmonics becomes more pronounced. At the same time, the shedding vortex from the upstream rotor impeller interacts with the downstream airfoil, resulting in increased vorticity at the top of the static airfoil and at the stator pressure surface. In addition, the dominant noise of the sound pressure level changes from third-order harmonic noise to BPF noise as the angle of attack increases.

(2) Experimental results with different numbers of rear guide vanes show that the harmonic noise of each order is affected by the stator. An even and dense increase in the guide vanes enhances the interaction between the rotor and the stator. This directly affects the amplitude and amount of tonal noise in the sound spectrum. On the other hand, irregularly distributed guide vanes suppress certain

noise spikes and reduce the amplitude of noise at BPF and harmonic frequencies.

(3) Numerical simulation results show that the low angle of attack leads to an increase in the separation flow at the tip of the impeller, which will result in a negative pressure region that will appear at the leading edge of the blades, which is considered to be a possible reason for the increase in noise at low angle of attack. The rotor blades periodically have an interference effect with the downstream stator. This causes the pressure on the near-wall surface of the blade to change periodically. In addition, numerical simulations observed that the 9-guide vane model has a higher total pressure while having a lower impact on the stator.

This study has identified that the dominant noise component changes with different angles of attack. Additionally, the uneven distribution of the rear guide vanes can effectively reduce the occurrence of single-tone noise while having a more powerful work capacity. Future research can focus on targeted noise reduction of the impeller under specific operating conditions, considering specific design requirements. The experimental and numerical simulation results presented in this paper provide insights into the relative positioning of vortex masses and airfoils under different flow conditions. Subsequent efforts will focus on optimizing the design of dynamic impeller blades, using specialized layouts to influence the distribution and development of vortex structures.

ACKNOWLEDGMENTS

The experiments are made possible through the joint support provided by the National Natural Science Foundation of China (Grant No.11972022), the Key Laboratory for Aerodynamic Noise Control (Grant No. ANCL20220204), China Aerodynamic Research & Development Centre and the Wenzhou Technologies R&D program of China (Grant No. G20240010), which are gratefully acknowledged.

CONFLICT OF INTEREST

No potential conflict of interest was reported by the authors.

AUTHORS CONTRIBUTION

Zhenghao Tu: Conceptualization, Software, Validation, Visualization, Writing - Original Draft, Investigation. **Yong Li**: Software, Formal analysis, Visualization, Methodology, Software, Validation, Formal analysis, Visualization. **Jianxi Zhou**: Conceptualization, Methodology, Validation, Formal analysis, Writing - Review & Editing, Funding acquisition. **Zhengwu Chen**: Supervision, Project administration.

REFERENCES

Benedek, T., & Vad, J. (2021). Beamforming based extension of semi-empirical noise modelling for low-speed axial flow fans. *Applied Acoustics, 178*, 108018. https://doi.org/10.1016/j.apacoust.2021.108018

Canepa, E., Cattanei, A., Jafelice, F., Zecchin, F. M., & Parodi, D. (2018). Effect of rotor deformation and blade loading on the leakage noise in low-speed axial fans. *Journal of Sound and Vibration, 433*, 99-123. https://doi.org/10.1016/j.jsv.2018.07.005

Čantrak, Đ. S., Janković, N. Z., & Ilić, D. B. (2015). Investigation of the turbulent swirl flow in pipe generated by axial fans using PIV and LDA methods. *Theoretical and Applied Mechanics, 42*(3), 211-222. https://doi.org/10.2298/TAM1503211C

Carolus, T., Schneider, M., & Reese, H. (2007). Axial flow fan broad-band noise and prediction. *Journal of sound and vibration, 300*(1-2), 50-70. https://doi.org/10.1016/j.jsv.2006.07.025

Chapman, G. T., & Yates, L. A. (1991). Topology of flow separation on three-dimensional bodies. *Applied Mechanics Reviews, 44*(7), 329-345. https://doi.org/10.1115/1.3119507

Han, T., & Patel, V. C. (1977). Flow-visualization of three-dimensional boundary-layer separation on bodies of revolution at incidence (No. 205). Iowa Institute of Hydraulic Research, University of Iowa. https://ui.adsabs.harvard.edu/abs/1977STIN...7813387H/abstract

Lewis, D., de Laborderie, J., Sanjosé, M., Moreau, S., Jacob, M. C., & Masson, V. (2021). Parametric study on state-of-the-art analytical models for fan broadband interaction noise predictions. *Journal of Sound and Vibration, 514*, 116423. https://doi.org/10.1016/j.jsv.2021.116423

Li, B., Lu, Q., Jiang, B., Yang, J., Wang, J., & Xie, J. (2022). Effects of outer edge bending on the aerodynamic and noise characters of axial fan for air conditioners. *Processes, 10*(4), 686. https://doi.org/10.3390/pr10040686

Liu, F., Wang, J. I. A. B. I. N. G., & Wu, K. E. Q. I. (2008). Numerical analysis of controlling separation in axial cascades by excitation of periodical incoming wake. *TASK Quarterly. Scientific Bulletin of Academic Computer Centre in Gdansk, 12*(1-2), 21-34. https://doi.journal.mostwiedzy.pl/TASKQuarterly/article/view/2047

Liu, H., Ouyang, H., Wu, Y., Tian, J., & Du, Z. (2014). Investigation of unsteady flows and noise in rotor-stator interaction with adjustable lean vane. *Engineering Applications of Computational Fluid Mechanics, 8*(2), 299-307. https://doi.org/10.1080/19942060.2014.11015515

Liu, X. (2018). *Aerodynamic and wake development of aerofoils with trailing-edge serrations* [Doctoral dissertation, University of Bristol]. https://research-information.bris.ac.uk/ws/portalfiles/portal/181451764/Final_Copy_2018_11_06_Liu_X_PhD.pdf

Longhouse, R. E. (1976). Noise mechanism separation and design considerations for low tip-speed, axial-flow fans. *Journal of Sound and Vibration*, *48*(4), 461-474. https://doi.org/10.1016/0022-460X(76)90550-2

Lu, H., Xiao, Y., Liu, Z., & Yuan, Y. (2022). Simulation and experimental research on aerodynamic noise of gas turbine 1.5-stage axial compressor. *Applied Acoustics*, *192*, 108722. https://doi.org/10.1016/j.apacoust.2022.108722

Lu, Z. (1991) A study on mode of 3-dimensional separation and open separation. Separated Flows and Jets: IUTAM-Symposium, Springer, 2018.04.043Berlin, Heidelberg. https://doi.org/10.1007/978-3-642-84447-8_32

Niu, X., Wang, X. N., & Li, Y. (2021). Numerical and experimental study for rotor-stator interaction noise of an axial fan. *Acta Aerodynamica Sinica*, *39*(5), 44-52. https://doi.org/10.1016/j.euromechflu.2021.02.004

Park, M., Lee, D. J., & Lee, H. (2022a). Inflow effects on tonal noise of axial fan under system resistances. *Applied Acoustics*, *192*, 108737. https://doi.org/10.1016/j.apacoust.2022.108737

Park, M., Lee, D. J., & Lee, H. (2022b). Tonal and broadband noise attenuation of an axial flow fan with forward and backward swept blades. *Applied Acoustics*, *195*, 108837. https://doi.org/10.1016/j.apacoust.2022.108837

Pereira, A., & Jacob, M. C. (2022). Modal analysis of in-duct fan broadband noise via an iterative Bayesian inverse approach. *Journal of Sound and Vibration*, *520*, 116633. https://doi.org/10.1016/j.jsv.2021.116633

Simonich, J. C., McCormick, D. C., & Lavrich, P. L. (1993). Role of leading-edge vortex flows in prop-fan interaction noise. *Journal of Aircraft*, *30*(2), 255-261. https://arc.aiaa.org/doi/abs/10.2514/3.48274?journalCode=ja

Wang, K. C. (1972). Separation patterns of boundary layer over an inclined body of revolution. *Aiaa Journal*, *10*(8), 1044-1050. https://www.sci-hub.ee/10.2514/3.50292

Ying, W. (2021). *High-order numerical simulations of broadband noise of turbulence-cascade interaction in aero-engines* [Doctoral dissertation]. https://doi.org/10.14711/thesis-991012936264003412

Zanon, A., De Gennaro, M., Kuehnelt, H., & Giannattasio, P. (2018). Assessment of the broadband noise from an unducted axial fan including the effect of the inflow turbulence. *Journal of Sound and Vibration*, *429*, 18-33. https://doi.org/10.1016/j.jsv.2018.04.043